


Dynamics of the Generation of Independent Orbital-Angular-Momentum Modes in a Photonic Chip

J.M. de Oliveira^{1,2,†}, J.C.A. Rocha,^{3,†} L.M.S. Santos,³ J.V.S. Moura,³ A.J. Jesus-Silva,³ and E.J.S. Fonseca^{3,*}

¹*Instituto Federal de Alagoas, Coruripe, Alagoas 57230-000, Brazil*

²*Programa de pós-graduação em Materiais, Universidade Federal de Alagoas, Maceió, Alagoas 57035-660, Brazil*

³*Instituto de Física, Universidade Federal de Alagoas, Maceió, Alagoas 57035-660, Brazil*

 (Received 3 February 2023; revised 8 June 2023; accepted 6 July 2023; published 2 August 2023)

The generation, propagation, and control of twisted light in a photonic chip has developed to meet the demands of modern optics, contributing to different research fields such as classical and quantum information technologies and integrated microfluidics. Here, we show how a single Gaussian illumination can excite different twisted-light modes into a buried annular waveguide, including that carrying orbital angular momentum (OAM) or superpositions of its constituents. We show that is possible to encode one-by-multiple information of independent OAM modes, unveiling the dynamics of the generation of OAM modes in a photonic chip. Owing to the degree of freedom of OAM light, OAM-circuit photonics can be explored to enhance high-capacity data processing for quantum or classical networking.

DOI: [10.1103/PhysRevApplied.20.024004](https://doi.org/10.1103/PhysRevApplied.20.024004)

I. INTRODUCTION

Light beams possessing orbital angular momentum (OAM) have recently been very widely explored in a variety of applications, ranging from quantum and classical communication [1–4] to optical trapping [5–7] and digital spiral imaging [8], just to cite some of the potential applications associated with the phase and intensity distribution of this particular class of light beam [9]. The diversity of application using beams carrying OAM is directly associated with their many intrinsic degrees of freedom and is mainly devoted to free space. However, recent years have seen a tremendous interest in the control of these degrees of freedom propagating within a waveguide such as optical fiber or even in photonic chips [10–12]. In fact, the combination of design and a high contrast in the refractive indices of the materials have permitted the optical fiber to support higher orders of OAM [13], with a high degree of purity [14], for long-distance applications [15]. These features allow the simultaneous transport of multiple independent OAM modes, scaling the transmission bandwidth by tailoring the spatial structure of the photons. On the other hand, an elaborate range of different waveguide designs have been projected to support light with OAM [16–19]; in

particular, waveguides embedded in a photonic chip written by a femtosecond-laser system [20–22], which offer the possibility of transmitting or emitting OAM modes longitudinally onto chips. Chen *et al.* [21] have shown output helical modes with a high degree of purity, faithfully mapping one-by-one OAM modes into and out of a photonic chip, but the authors have not explored the dependence of the output OAM modes on the tuning of the input modes. Oliveira *et al.* [22] have presented the generation and guiding of optical beams carrying OAM with a tunable topological charge, demonstrating the possibility of controlling the output OAM modes by tuning the input-beam coupling. However, the resulting output modes are not pure enough because of the waveguide's own written structure.

At the present work, we explore how a single Gaussian illumination can select and excite a single OAM mode, or even a superposition of OAM modes, with a high degree of purity in a waveguide by arranging its illumination input parameters. Here, we advance physical insights into the coupling and dynamics of the propagation inside the photonic chip. Our findings may represent an important step forward in obtaining a pure OAM mode by exciting it, in a waveguide, in a proper way, thus being fundamental to the exploration of the interplay between the transverse spatial modes and evanescent coupling between waveguides. Our experimental results are supported by numerical simulations.

*eduardo@fis.ufal.br

†These authors contributed equally to this work.

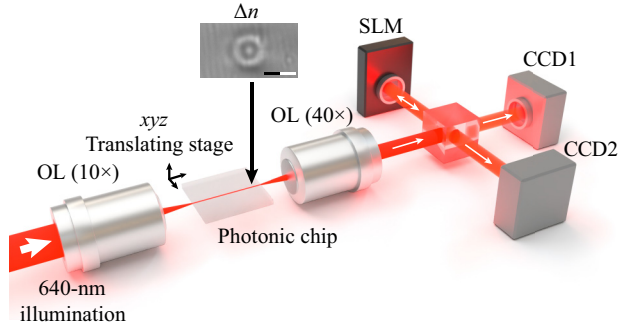


FIG. 1. The experimental setup. The inset shows an optical-microscopic image of the waveguide transverse profile. The scale bar is 10 μm .

II. MATERIALS AND METHODS

A femtosecond-laser writing system [23] was used for modifying the refractive index of boro-aluminosilicate glassy blades and building “donut-shaped” waveguides. A cylindrical lens pair was responsible for shaping the incident femtosecond-laser-beam profile, ensuring rotational symmetry of the modification along the writing direction [24]. A set of 19 tracks was used for precisely structuring a cylindrical symmetric 10- μm -diameter and 20-mm-long waveguide (Fig. 1, inset). For this work, we wrote “donut-shaped” waveguides with the same dimensions but slightly different writing pulse energies, of 300 nJ and 350 nJ, termed WG_1 and WG_2 , respectively. Both cases resulted in refractive-index changes of the order of 10^{-3} and negligible birefringence.

Figure 1 shows the experimental setup for the intensity-profile recording and projection measurements. By means of an *end-fire* coupling system, a Gaussian beam mode is coupled into the waveguide and the output mode is tuned by carefully controlling the beam-traversal displacement and inclination relative to the coupling axis of the photonic chip, using an xyz stage and a mirror (not shown) positioned before the objective lens OL (10 \times) [22]. The output OAM mode is directed to a beam splitter, where half of the beam intensity goes to camera CCD1, to record the output profile, while the other half shines onto a phase-only spatial light modulator (SLM). In the SLM, we place a phase mask of a spiral phase step that undergoes a phase shift from 0 to $2m'\pi$, where m' is the topological charge. Once a spiral phase mask is imprinted in the SLM and has an opposite charge to the field output from the waveguide, the vortex at the center will be cancelled and an intensity maximum is expected to be observed in the center of the far field after the SLM, using camera CCD2. Measurements are made simultaneously on both cameras, meaning that we measure the output mode using CCD1 and projective measurements of that same mode using CCD2. In order to measure the power spectra, we have to quantify the relative

intensity at the beam center for several possible topological charges in the SLM. To better understand this concept, suppose that the output state can be written as

$$\Psi_{\text{out}}(r, \phi) = \sum_m A_m(r) e^{im\phi}, \quad (1)$$

where we assume a radially symmetric amplitude $A_m(r)$, m is the OAM topological charge associated with this amplitude distribution, r and ϕ are the radial and polar coordinates, respectively.

The SLM acts as a phase flattener when it imprints in the field the phase shift $\Phi(\phi) = \exp[im'\phi]$ for a certain value of m' . The field reflected from the SLM at the SLM plane is given by $\Psi_{\text{out}}\Phi$. To express the field in the far plane in terms of the field in the SLM plane, we calculate a Fourier transform that describes the Fraunhofer diffraction,

$$\begin{aligned} \Psi_{\text{out}}\Phi &= \left[\sum_m A_m(r) e^{im\phi} \right] e^{im'\phi} \rightarrow \\ &= \int_0^{2\pi} \int_0^\infty \sum_m A_m(r) e^{im\phi} e^{im'\phi} e^{-i2\pi rk \cos(\phi_k - \phi)} r dr d\phi, \end{aligned} \quad (2)$$

in which (r, ϕ) are the spatial coordinates at the plane of the SLM and (k, ϕ_k) are the spatial coordinates in the far plane. Taking this result at the center corresponds to setting $k = 0$ in the above integral. Therefore, the ϕ integral is easily evaluated, resulting in a Kronecker delta $\delta_{-m, m'}$, and the far field at the center will have a non-null contribution proportional to

$$\left| \int_0^\infty A_{-m'}(r) r dr \right|^2. \quad (3)$$

This contribution will produce an intensity maximum in the center when the topological charge is exactly cancelled ($m' = -m$) [25]. The maximum is proportional to the net amplitude of the corresponding mode in the mode superposition of Eq. (1); therefore, by using different masks in the SLM, we can obtain the OAM spectrum as shown in Fig. 5.

III. RESULTS AND DISCUSSION

For the numerical results, we solve the scalar paraxial wave equation using the alternating-direction-implicit finite-difference (ADI-FD) scheme [26], with perfectly matched layers on the boundaries to prevent reflections from outgoing waves [26,27].

Figure 2 shows numerically how the input-illumination configuration and the relative refractive index Δn excite different output modes, including OAM-carrying ones. Figure 2(a) illustrates the evolution dynamics from outside

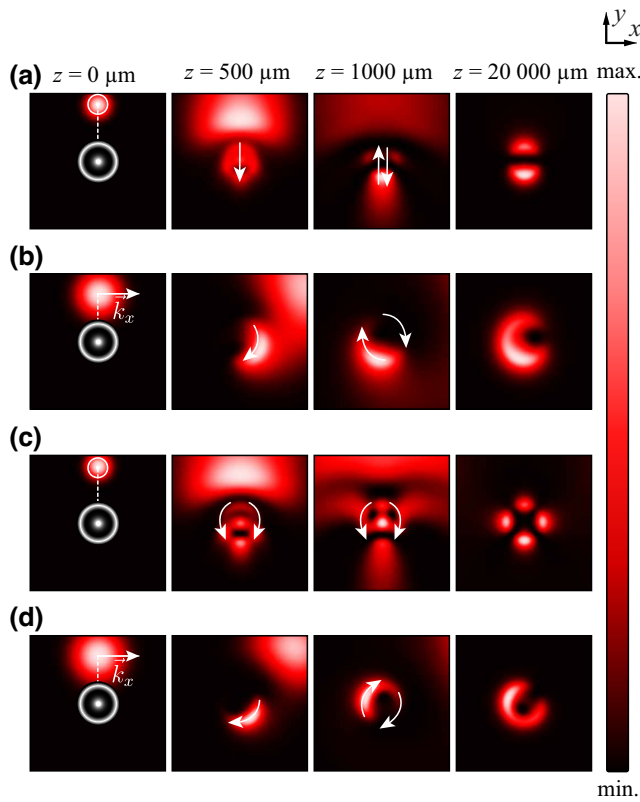


FIG. 2. The numerical simulation of OAM modes into the waveguide for different input-coupling configurations and refractive-index changes Δn . (a) The Gaussian light couples parallel to the waveguide axis. After diffraction, the resultant field inside the waveguide is a superposition of modes $m = 1$ and $m = -1$. (b) The incident Gaussian light has a transversal displacement, given by the wave vector \vec{k}_x . The resultant mode is $m = 1$. In (a) and (b), the refractive-index change is $\Delta n = 1.2 \times 10^{-3}$. In (c) and (d), the input coupling is similar to that in (a) and (b) but the refractive index is increased to $\Delta n = 2.2 \times 10^{-3}$. In (c), the resultant mode is the superposition of modes $m = 2$ and $m = -2$ and in (d) the resultant mode is $m = 2$. Each initial condition can be defined by the beam waist, w_0 , the beam transversal distance to the waveguide z axis, d , and the angle that the beam makes relative to the waveguide z axis, θ . For (a) and (c), we have $w_0 = 4 \mu\text{m}$, $d = 14 \mu\text{m}$, and $\theta = 0^\circ$. For (b) and (d), we have $w_0 = 6 \mu\text{m}$, $d = 10 \mu\text{m}$, and $\theta = 1.5^\circ$. The distances from the initial plane, from the left column to the right column, are $z = 0, 500, 1000, 20\,000 \mu\text{m}$.

to inside of the waveguide for a single external Gaussian illumination (red profile), with the wave vector parallel to the waveguide direction coming to meet the waveguide (white circle with a dot in the center). The Gaussian beam expands due to diffraction and couples with the waveguide, forming waves going in opposite transverse directions, which interfere and form bright and dark regions. Finally, we have a stable superposition of OAM modes $m = 1$ and $m = -1$, represented in the last column, corresponding to the waveguide output. Figure 2(b) illustrates the evolution

dynamics for a Gaussian input beam with a transversal wave-vector component \vec{k}_x ($\vec{k}_x = \vec{k} \sin\theta$), as depicted with a white arrow. The Gaussian beam couples with the upper side of the waveguide, which holds that wave and carries it circularly. In this configuration, the resultant mode carries OAM with topological charge strength $m = 1$. It is important to draw attention to the fact that higher values of refractive-index changes inside the waveguide can couple different propagating OAM modes [28]. This can be observed in Figs. 2(c) and 2(d), where we have a superposition of modes with $m = 2$ and $m = -2$ [Fig. 2(c)] and a resultant mode with $m = 2$ in (d), in which we have used the same initial conditions as Figs. 2(a) and 2(b), respectively, but increased the waveguide refractive-index change from $\Delta n = 1.2 \times 10^{-3}$ to $\Delta n = 2.2 \times 10^{-3}$. Videos of the entire propagation, with additional phase plots, are provided in the Supplemental Material [29], using the same labeling as in Fig. 2 for each respective initial condition.

The spatial parameters of how the light couples with the waveguide play an important role in determining which modes are generated. To implement an experimental procedure, we follow the input coupling represented in Figs. 3(a), 3(c), and 3(e). Figure 3(a) represents the source of illumination relative to the center of the waveguide and its direction, parallel to the waveguide (transversal wave vectors $\vec{k}_x = 0$). Different initial illumination conditions, labeled with numbers from 1 to 4, were used to generate the numerical and experimental results shown in Fig. 3(b). It is clearly observed that the input mode has evolved to the superposition of modes with $m = 1$ and $m = -1$ according to the input coupling labeled in Fig. 3(a). All of the modes represented in Figs. 3(b), 3(d), and 3(f) correspond to output modes from the waveguide. In the experiment, these modes are directly imaged to CCD1 to produce the presented experimental results.

Still in Fig. 3, the OAM modes $m = -1$ and $m = 1$, besides the Gaussian mode $m = 0$, are generated by considering Figs. 3(c) and 3(e), where the transverse movement of the beam comes into play due to a transversal wave-vector component, \vec{k}_x . We consider three different situations. In Fig. 3(c), we consider an initial Gaussian beam with an angle of $\theta = 1^\circ$ relative to the waveguide longitudinal axis, z . The labels 1 and 2 in Fig. 3(c) depict the generation of $m = +1$ and $m = -1$, respectively. Interestingly, the signal of the OAM mode is dependent on the input-coupling propagation direction. In Fig. 3(e), the Gaussian mode was aligned at the center of the waveguide in order to obtain the output mode $m = 0$ [Fig. 3(f)]. These numerical and experimental results agree with the refractive-index change $\Delta n = 1.2 \times 10^{-3}$, achieved by 300 nJ of incident energy during waveguide fabrication.

Now, by increasing the laser power on the writing system, the WG₂ waveguide presents a higher

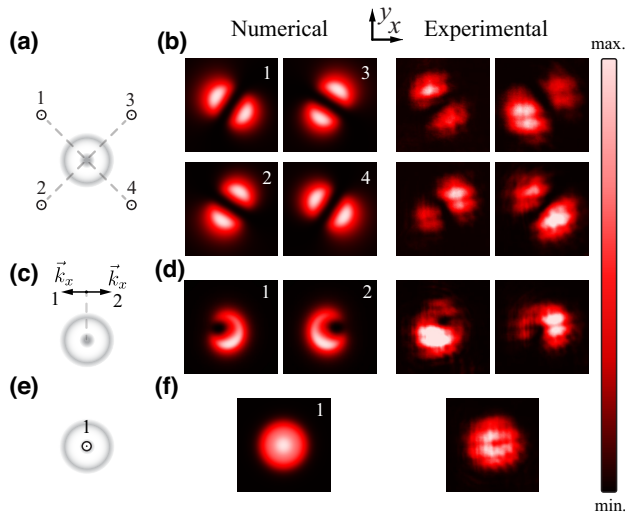


FIG. 3. The generation of modes for the WG_1 waveguide, written with 300 nJ of incident energy. In (a), (c), and (e), we show the source-illumination initial conditions at different center points and directions relative to the waveguide longitudinal axis for (b), (d), and (f), respectively, with labels for each case. (b) Numerical and experimental results depicting the output superposition of OAM modes $m = \pm 1$ with illumination at the source points shown in (a). (d) Numerical and experimental results depicting the generation of OAM-carrying modes from illumination at different source points and directions [according to (c)], exploring the effect of the lateral movement of the initial beam. The source illumination to generate the modes in (d) is a Gaussian beam with angle $\theta = 1.0^\circ$, relative to the waveguide longitudinal axis, with a direction depicted in the corresponding diagram at (c). The direction labeled as 1 generates the corresponding OAM modes $m = +1$ depicted in the first and third columns, while the OAM modes $m = -1$ shown in the second and fourth columns are generated with the direction labeled as 2. Lastly, in (f), we show the generation of the fundamental waveguide mode when the source illumination is centered and parallel to the waveguide longitudinal axis.

refractive-index change. Figure 4 shows the numerical and experimental results for the new waveguide. Figures 4(a), 4(c), 4(e), and 4(g) correspond to the illumination configuration used to obtain the results presented in Figs. 4(b), 4(d), 4(f), and 4(h), respectively. All of the modes represented in Figs. 4(b), 4(d), 4(f), and 4(h) correspond to output modes from the waveguide, which are directly imaged to CCD1 to produce the experimental results. In Fig. 4(b), we now have a superposition of OAM modes with $m = -2$ and $m = 2$. It is clearly observed that the new waveguide supports higher OAM modes than those of Fig. 3. It is worth noting that different OAM modes can be accessed with different angles of incidence θ [Figs. 4(c)–4(f)]. To generate the modes $m = \pm 2$, we have used $\theta = 1.5^\circ$, while to generate modes $m = \pm 1$, we have used a lower angle, $\theta = 0.5^\circ$, which translates into a lower-magnitude transversal wave vector \vec{k}_x . In Fig. 4(h), we

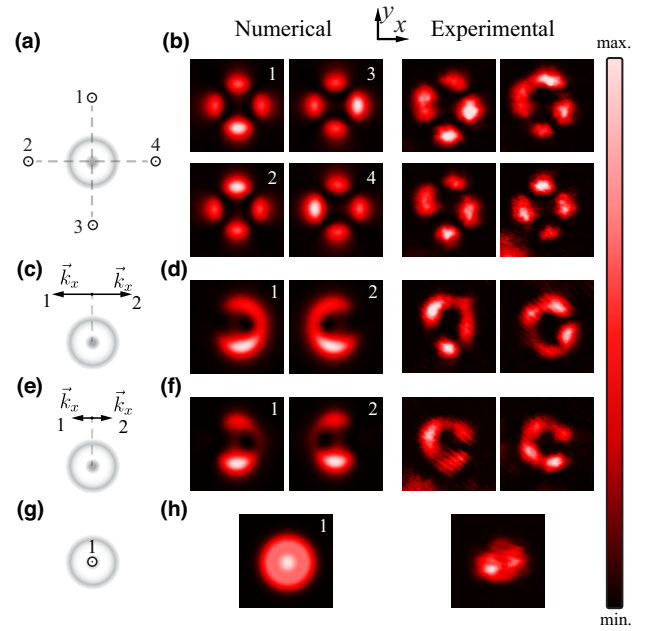


FIG. 4. The generation of modes for the WG_2 waveguide, written with 350 nJ of incident energy. Diagrams (a), (c), (e), and (g) show the source-illumination initial conditions at different center points and directions relative to the waveguide longitudinal axis for (b), (d), (f), and (h), respectively, with labels for each case. (b) Numerical and experimental results depicting the output superposition of OAM modes $m = \pm 2$ with illumination at various source points. (d),(f) Numerical and experimental results depicting the generation of OAM-carrying modes from illumination at different source points and in different directions, exploring the effect of lateral movement of the initial beam. The source illumination to generate the modes in (d) is a Gaussian beam with angle $\theta = 1.5^\circ$, relative to the waveguide longitudinal axis, with the direction depicted in the corresponding diagram at (c). The direction labeled as 1 generates the corresponding OAM modes $m = +2$ depicted in the first and third columns, while the OAM modes $m = -2$ shown in the second and fourth columns are generated with the direction labeled as 2. (f) Similarly, but with a different angle $\theta = 0.5^\circ$, we show the generation of OAM modes $m = \pm 1$. (h) Lastly, we show the generation of the fundamental waveguide mode when the source illumination is centered and parallel to the waveguide longitudinal axis.

generate the fundamental waveguide mode when sending light parallel to the waveguide and centered with it. Once more, the numerical and experimental results agree with a refractive-index change of $\Delta n = 2.2 \times 10^{-3}$ for the WG_2 waveguide.

An important point at this stage is to characterize the degree of purity of the output modes. Figure 5 corresponds to the output OAM power spectra to the different input configurations related to Figs. 3 and 4. To obtain these results, instead of imaging the waveguide output to CCD1, it is imaged over the SLM and the reflected image will propagate to CCD2, which will register the far field. In that

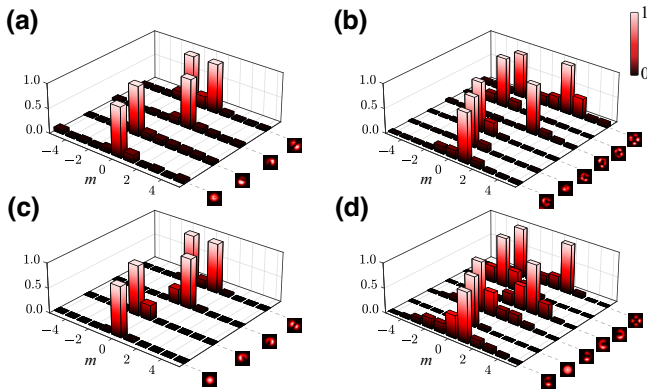


FIG. 5. Projective measurements depicting the OAM spectrum for different output modes and waveguides. (a),(c) In the left column, we have the spectrum of the output modes for the WG₁ waveguide: (a) experimental; (c) numerical. (b),(d) In the right column, we have the projective measurements for the output modes from the waveguide that support higher-order modes (WG₂) and we show a richer set of modes and their OAM spectra: (b) experimental; (d) numerical. In all cases, there is good agreement between experiment and theory, and the expected mode OAM spectrum.

case, for each azimuthal phase displayed in the SLM, the maximum at the center of the intensity pattern in CCD2 will indicate the OAM content of the field. These results highlight that independent modes can propagate into the photonic chip by tuning only one Gaussian-illumination input, leading to the possibility of controlling a unique output mode. This high selectivity is very important in mode-division multiplexing (MDM) systems, since OAM data encoding depends on the maintenance of intermodal orthogonality and reduced interchannel crosstalk [30].

As we have already pointed out, the prerequisite of controlling OAM modes inside a photonic chip is not so straightforward. The waveguide's own fabrication parameters, such as the pulse energy, scan velocity, annular profile symmetry, voxel shape, and diameter [20,28,31], are fundamental to assure the proper propagation of modes inside the annular waveguide. For example, it is known that the regime of propagation (scalar or vectorial), as well as the supported modes, are strongly dependent on the material substrate and the irradiation conditions during the laser modification [20,24]. In our case, both the borosilicate glass and the writing laser fluence are adequate for generating waveguides with negligible birefringence and low refractive-index change [22,24]. Furthermore, the numerical simulation clearly shows that the excitation of the possible modes depends on, at least, two coupling parameters adjusted relative to the waveguide longitudinal axis: (i) the input-beam direction, depicted by the transversal wave vector \vec{k}_τ ; and (ii) the beam transverse offset (x, y) .

As discussed in our previous work [22], we had experimentally verified a very close relation between the phase shift imposed by offset coupling and the topological charge of the OAM-possessing beams guided or excited by the annular waveguide. However, it had not been possible to understand exactly how those vortex beams would be generated. But now, from numerical-simulation point of view, we can clearly see the wavefront diffracting and coupling the annular waveguide in an unconventional manner, holding the light beam in a spiraling trajectory inside the cylindrical structure. Indeed, the direction of the transversal component of the wave vector \vec{k} is responsible for breaking the rotational symmetry of the system and introducing a preferred direction of rotation, differentiating the OAM+ or OAM- modes.

Interestingly enough, Chen *et al.* [21] have mapped one-by-one OAM modes into and out of a photonic chip with a high degree of purity. Here, we excite the desired output pure mode, even one superposition, by tuning only one coupling mode, a Gaussian mode, but not restricting to it. This significantly expands the control over twisted light within integrated photonics, enabling the integration of high-dimensional information processing [32]. Additionally, this level of control could open up new possibilities for interferometric processes using spatial modes within a photonic chip [33].

IV. CONCLUSIONS

To conclude, we have experimentally and numerically demonstrated the generation of OAM modes and their superpositions within the same waveguide through a precisely tuned single Gaussian-illumination input. By controlling the angle of incidence of the input light relative to the waveguide longitudinal axis, the dynamics of OAM-mode generation in a photonic chip have also been unveiled. The choice of the writing parameters and the control of the coupling settings guarantee the high selectivity of the modes. In fact, a notable feature of our photonic chip is that, by maintaining a consistent set of waveguide-fabrication parameters, including the pulse energy, the scan velocity, the symmetry of the annular profile, and the voxel shape, it is possible to achieve a desired output mode simply by adjusting the input light parameters. Our photonic chip has the potential to be employed in a range of settings, including quantum and classical communication and microfluidic systems [34–37]. Moreover, understanding the coupling dynamics and mode tuning within the same waveguide might allow for the construction of fully OAM photonic circuits.

ACKNOWLEDGMENTS

The present research was supported by the Instituto Nacional de Ciência e Tecnologia de Informação Quântica [CNPq INCT-IQ (Grant No. 465469/2014-0)], the

Fundação de Amparo à Pesquisa do estado de Alagoas (FAPEAL), the Conselho Nacional de Desenvolvimento Científico e Tecnológico (CNPq), and the Coordenação de Aperfeiçoamento de pessoal de Nível Superior, Finance Code No. 001 (CAPES).

- [1] G. Gibson, J. Courtial, M. J. Padgett, M. Vasnetsov, V. Pas'ko, S. M. Barnett, and S. Franke-Arnold, Free-space information transfer using light beams carrying orbital angular momentum, *Opt. Express* **12**, 5448 (2004).
- [2] J. Wang, J.-Y. Yang, I. M. Fazal, N. Ahmed, Y. Yan, H. Huang, Y. Ren, Y. Yue, S. Dolinar, and M. Tur, *et al.*, Terabit free-space data transmission employing orbital angular momentum multiplexing, *Nat. Photon.* **6**, 488 (2012).
- [3] J. T. Barreiro, T.-C. Wei, and P. G. Kwiat, Beating the channel capacity limit for linear photonic superdense coding, *Nat. Phys.* **4**, 282 (2008).
- [4] Y. Chen, S. Liu, Y. Lou, and J. Jing, Orbital Angular Momentum Multiplexed Quantum Dense Coding, *Phys. Rev. Lett.* **127**, 093601 (2021).
- [5] M. P. MacDonald, L. Paterson, K. Volke-Sepulveda, J. Arlt, W. Sibbett, and K. Dholakia, Creation and manipulation of three-dimensional optically trapped structures, *Science* **296**, 1101 (2002).
- [6] Y. Yang, Y. Ren, M. Chen, Y. Arita, and C. Rosales-Guzmán, Optical trapping with structured light: A review, *Adv. Photon.* **3**, 034001 (2021).
- [7] D. G. Grier, A revolution in optical manipulation, *Nature* **424**, 810 (2003).
- [8] L. Torner, J. P. Torres, and S. Carrasco, Digital spiral imaging, *Opt. Express* **13**, 873 (2005).
- [9] H. Rubinsztein-Dunlop, A. Forbes, M. V. Berry, M. R. Dennis, D. L. Andrews, M. Mansuripur, C. Denz, C. Alpmann, P. Banzer, and T. Bauer, *et al.*, Roadmap on structured light, *J. Opt.* **19**, 013001 (2016).
- [10] H. Yang, Z. Xie, H. He, Q. Zhang, and X. Yuan, A perspective on twisted light from on-chip devices, *APL Photon.* **6**, 110901 (2021).
- [11] S. Li, Q. Mo, X. Hu, C. Du, and J. Wang, Controllable all-fiber orbital angular momentum mode converter, *Opt. Lett.* **40**, 4376 (2015).
- [12] S. Ramachandran and P. Kristensen, Optical vortices in fiber, *Nanophotonics* **2**, 455 (2013).
- [13] C. Brunet, P. Vaity, Y. Messaddeq, S. LaRochelle, and L. A. Rusch, Design, fabrication and validation of an OAM fiber supporting 36 states, *Opt. Express* **22**, 26117 (2014).
- [14] Z. Zhang, J. Gan, X. Heng, Y. Wu, Q. Li, Q. Qian, D. Chen, and Z. Yang, Optical fiber design with orbital angular momentum light purity higher than 99.9%, *Opt. Express* **23**, 29331 (2015).
- [15] A. Wang, L. Zhu, L. Wang, J. Ai, S. Chen, and J. Wang, Directly using 8.8-km conventional multi-mode fiber for 6-mode orbital angular momentum multiplexing transmission, *Opt. Express* **26**, 10038 (2018).
- [16] D. Pan, H. Wei, L. Gao, and H. Xu, Strong Spin-Orbit Interaction of Light in Plasmonic Nanostructures and Nanocircuits, *Phys. Rev. Lett.* **117**, 166803 (2016).
- [17] M. J. Strain, X. Cai, J. Wang, J. Zhu, D. B. Phillips, L. Chen, M. Lopez-Garcia, J. L. O'Brien, M. G. Thompson, and M. Sorel, *et al.*, Fast electrical switching of orbital angular momentum modes using ultra-compact integrated vortex emitters, *Nat. Commun.* **5**, 1 (2014).
- [18] J. Zhang, C. Sun, B. Xiong, J. Wang, Z. Hao, L. Wang, Y. Han, H. Li, Y. Luo, and Y. Xiao, *et al.*, An InP-based vortex beam emitter with monolithically integrated laser, *Nat. Commun.* **9**, 1 (2018).
- [19] W.-Y. Tsai, Q. Sun, G. Hu, P. C. Wu, R. J. Lin, C.-W. Qiu, K. Ueno, H. Misawa, and D. P. Tsai, Twisted surface plasmons with spin-controlled gold surfaces, *Adv. Opt. Mater.* **7**, 1801060 (2019).
- [20] Y. Chen, K.-Y. Xia, W.-G. Shen, J. Gao, Z.-Q. Yan, Z.-Q. Jiao, J.-P. Dou, H. Tang, Y.-Q. Lu, and X.-M. Jin, Vector Vortex Beam Emitter Embedded in a Photonic Chip, *Phys. Rev. Lett.* **124**, 153601 (2020).
- [21] Y. Chen, J. Gao, Z.-Q. Jiao, K. Sun, W.-G. Shen, L.-F. Qiao, H. Tang, X.-F. Lin, and X.-M. Jin, Mapping Twisted Light into and out of a Photonic Chip, *Phys. Rev. Lett.* **121**, 233602 (2018).
- [22] J. M. de Oliveira, L. M. S. Santos, A. J. Jesus-Silva, and E. J. S. Fonseca, Tunable generation and propagation of vortex beams in a photonic chip, *Phys. Rev. A* **104**, L061501 (2021).
- [23] J. M. Oliveira, A. J. Jesus-Silva, A. C. Silva, N. O. Dantas, and E. J. Fonseca, Waveguides written in silver-doped tellurite glasses, *Opt. Mater. (Amst)* **101**, 109767 (2020).
- [24] G. Corrielli, A. Crespi, R. Geremia, R. Ramponi, L. Sansoni, A. Santinelli, P. Mataloni, F. Sciarrino, and R. Osellame, Rotated waveplates in integrated waveguide optics, *Nat. Commun.* **5**, 1 (2014).
- [25] H. Qassim, F. M. Miatto, J. P. Torres, M. J. Padgett, E. Karimi, and R. W. Boyd, Limitations to the determination of a Laguerre-Gauss spectrum via projective, phase-flattening measurement, *J. Opt. Soc. Am. B* **31**, A20 (2014).
- [26] G. L. Pedrola, *Beam Propagation Method for Design of Optical Waveguide Devices* (John Wiley & Sons, Chichester, United Kingdom, 2015).
- [27] W. Huang, C. Xu, W. Lui, and K. Yokoyama, The perfectly matched layer (PML) boundary condition for the beam propagation method, *IEEE Photon. Technol. Lett.* **8**, 649 (1996).
- [28] R. Ismaeel, T. Lee, B. Oduro, Y. Jung, and G. Brambilla, All-fiber fused directional coupler for highly efficient spatial mode conversion, *Opt. Express* **22**, 11610 (2014).
- [29] See the Supplemental Material at <http://link.aps.org/supplemental/10.1103/PhysRevApplied.20.024004> for videos of the entire propagation inside the waveguide, with additional phase plots.
- [30] S. Restuccia, D. Giovannini, G. Gibson, and M. Padgett, Comparing the information capacity of Laguerre-Gaussian and Hermite-Gaussian modal sets in a finite-aperture system, *Opt. Express* **24**, 27127 (2016).
- [31] W.-G. Shen, Y. Chen, H.-M. Wang, and X.-M. Jin, OAM mode conversion in a photonic chip, *Opt. Commun.* **507**, 127615 (2022).

- [32] H. Bechmann-Pasquinucci and W. Tittel, Quantum cryptography using larger alphabets, *Phys. Rev. A* **61**, 062308 (2000).
- [33] A. Mohanty, M. Zhang, A. Dutt, S. Ramelow, P. Nussenzweig, and M. Lipson, Quantum interference between transverse spatial waveguide modes, *Nat. Commun.* **8**, 1 (2017).
- [34] A. E. Willner, H. Song, K. Zou, H. Zhou, and X. Su, Orbital angular momentum beams for high-capacity communications, *J. Lightwave Technol.* **41**, 1918 (2023).
- [35] M. Lian, L. Mao, Z. Li, Z. Liu, Z. Wang, and T. Cao, Reconfigurable size-sorting of micronanoparticles in chalcogenide waveguide array, *Adv. Photon. Res.* **3**, 2200078 (2022).
- [36] N. M. Kerschbaumer, L. I. Fochler, M. Reichenspurner, S. Rieger, M. Fedoruk, J. Feldmann, and T. Lohmüller, Twisted light Michelson interferometer for high precision refractive index measurements, *Opt. Express* **30**, 29722 (2022).
- [37] M. Zahidy, Y. Liu, D. Cozzolino, Y. Ding, T. Morioka, L. K. Oxenløwe, and D. Bacco, Photonic integrated chip enabling orbital angular momentum multiplexing for quantum communication, *Nanophotonics* **11**, 821 (2022).